A Solution-processed Inorganic Emitter with High Spectral Selectivity for Efficient Subambient Radiative Cooling in Hot Humid Climates

Chongjia Lin, Yang Li, Cheng Chi, Ye Seul Kwon, Jingyuan Huang, Zuoxu Wu, Jiongzhi Zheng, Gongze Liu, Chi Yan Tso, Christopher Y. H. Chao[*]*, and Baoling Huang*[*]

Dr. C. Lin, Dr. Y. Li, Y. S. Kwon, J. Huang, J. Zheng, G. Liu, Prof. B. Huang

Department of Mechanical and Aerospace Engineering, The Hong Kong University of Science and Technology, Clear Water Bay, Kowloon, Hong Kong

E-mail: mebhuang@ust.hk

Dr. C. Chi

Key Laboratory for Thermal Science and Power Engineering of Ministry of Education, Department of Engineering Mechanics, Tsinghua University, Beijing, China

Z. Wu

School of Science, Harbin Institute of Technology, Shenzhen, China

Prof. C. Y. Tso

School of Energy and Environment, City University of Hong Kong, Kowloon, Hong Kong

Prof. C. Y. H. Chao

This article has been accepted for publication and undergone full peer review but has not been through the copyediting, typesetting, pagination and proofreading process, which may lead to differences between this version and the Version of Record. Please cite this article as doi: 10.1002/adma.202109350.

WILEY-VCH

Department of Building Environment and Energy Engineering and Department of Mechanical Engineering, The Hong Kong Polytechnic University, Hong Kong

E-mail: christopher.chao@polyu.edu.hk

Keywords: inorganic emitter, selective thermal emission, subambient radiative cooling, hot humid climates, cooling temperature

Abstract

Daytime radiative cooling provides an eco-friendly solution to space cooling with zero energy consumption. Despite significant advances, most state-of-the-art radiative coolers show broadband infrared emission with low spectral selectivity, which limits their cooling temperatures, especially in hot humid regions. Here we report an all-inorganic narrowband emitter comprising a solution-derived SiO_xN_y layer sandwiched between a reflective substrate and a self-assembly monolayer of SiO_2 microspheres. It shows a high and diffusive solar reflectance (96.4%) and strong infrared-selective emittance (94.6%) with superior spectral selectivity (1.46). Remarkable subambient cooling of up to 5 °C in autumn and 2.5 °C in summer are achieved under high humidity without any solar shading or convection cover at noontime in a subtropical coastal city, Hong Kong. Owing to the all-inorganic hydrophobic structure, the emitter shows outstanding resistance to ultraviolet and water in the long-term durability tests. The scalable solution-based fabrication renders this stable high-performance emitter promising for large-scale deployment in various climates.

1. Introduction

Passive radiative cooling, in which heat is spontaneously radiated by surfaces to the higher sky with a low temperature through the atmospheric infrared (IR) windows, provides a sustainable solution to space cooling with zero energy consumption.[1] Although nighttime cooling has been utilized for centuries, it was only recently that noontime cooling was first demonstrated using a multilayer photonic structure. [2] In tropical and subtropical areas, the demand for cooling is particularly huge due to high ambient temperatures. However, it has proved difficult to achieve daytime cooling in such areas with stronger solar irradiation and higher humidity than mid-latitude regions.[3-7] With the

increase in humidity, the transmittances within the atmospheric windows remarkably decrease while most secondary windows such as the 16-25 μm window may even disappear in humid climates (Figure S1). This significantly increases the atmospheric radiation and limits the cooling capability of radiative coolers, especially those with strong IR absorption/emission beyond the major atmospheric window. Although broadband IR emitters may provide ~10% higher cooling power potential than selective ones in less humid climates due to the existence of secondary windows, in humid areas with high precipitable water vapor (PWV), this advantage vanishes and their cooling temperatures are notably limited by broadband IR absorption.[8] To maintain applicability in different climates, an ideal daytime radiative cooler should show high emittance only within the main 8-13 μm atmospheric window ($\varepsilon_{8\text{-}13\mu m}$), which is less sensitive to moisture, to maximize emission power, but high reflectance R beyond this window to minimize the received radiation from the atmosphere and surroundings, i.e., a narrowband IR emission with high spectral selectivity $\eta_\varepsilon = \varepsilon_{8\text{-}13\mu m} / \varepsilon_{0\text{-}\infty\mu m.}$[2, 9-12]

Over the past few years, significant efforts have been made to improve daytime radiative cooling performance and reduce costs.[11, 13-16] The noontime radiative cooling was first achieved with a multilayer photonic crystal,[2] showing a high R_{solar} = 97%, reasonable $\varepsilon_{8\text{-}13\mu m}$ = 65% and a high η_ε = 1.48. Later on, other multilayer emitters[10, 17-19] with improved $\varepsilon_{8\text{-}13\mu m}$ were developed, but their large-scale deployment was restricted by high fabrication costs. Thus, scalable designs adopting dispersed inorganic particles,[20-22] porous polymers[23] and even woods[24] were developed to achieve both high R_{solar} (>94%) and high $\varepsilon_{8\text{-}13\mu m}$ (>90%). These low-cost emitters enable the practical applications of daytime radiative cooling, but they normally show broadband IR emission and low η_ε (~1). Meanwhile, they often adopt polymer matrices, of which the potential aging issue caused by the exposure to ultraviolet and moisture should be addressed for long-time applications.[25] Hence, it is urgently demanded to develop scalable IR-selective radiative coolers with great long-term stability in the harsh outdoor environment.

Here we demonstrate a robust all-inorganic narrowband emitter with strong diffusive solar reflection (R_{solar} = 96.4%) and highly selective IR emission ($\varepsilon_{8\text{-}13\mu m}$ = 94.6%), which can be fabricated by scalable solution processes at room temperature. Its high IR emittance mainly locates within the major atmospheric window, leading to a high spectral selectivity η_ε = 1.46, which is the highest among state-of-the-art emitters with comparable $\varepsilon_{8\text{-}13\mu m}$. Temperature drops of 5 °C in autumn and 2.5 °C in

summer were achieved in a humid subtropical coastal city, Hong Kong, with the emitter directly exposed to sunlight at noontime without adopting any solar shading structure or convection cover. The selective emitter consistently showed 40% higher cooling temperature than non-selective one in the comparison test. Moreover, the inorganic cooler exhibited exceptional long-term stability after ultraviolet exposure (3 months) and water immersion (3 weeks), which is critical for practical deployments.

2. Results and Discussion

2.1. The Structure of the Emitter and its Spectrum

The emitter has a triple-layer structure, comprising a monolayer of closely packed silica microspheres, a silicon oxynitride (SiO_xN_y) layer derived from perhydropolysilazane (PHPS) and a silver layer on a substrate (**Figure 1**b-c**)**. This simple all-inorganic design can generate highly selective but strong IR emission (Figure 1a) by rationally exploiting the optical behaviors of the SiO_xN_y layer and silica microspheres.

The emitter was fabricated using facile solution processes (Figure 1e). PHPS, an inorganic precursor containing Si-N skeleton, was used to generate a dense SiO_xN_y layer on a silver-coated substrate through natural solidification at room temperature (Figure S2, S3 and S4). Although the N-content of SiO_xN_y layer affects the emissive spectrum and it can be controlled by curing temperature or special environments,[26-29] solidification in the air at room temperature meets our demands of both good spectral selectivity and low fabrication cost. The SiO_xN_y/Ag structure was mirror-like and showed highly selective IR emission ($\varepsilon_{8\text{-}13\mu m} \approx 80\%$ and $\eta_\varepsilon > 1.4$). Another emissive peak caused by Si-H bonds[30] was observed at 4.63 μm, which matches the 4.5-5 μm atmospheric window. It is worth noting that although SiO_xN_y films and SiO_2/Si_3N_4 multilayer structures deposited using vacuum technologies have been used to produce selective emission,[31, 32] their spectra are significantly different from this solution-processed film, and they should be considered as optically different materials. To enhance its IR emissivity while maintaining the spectral selectivity, a monolayer of SiO_2 microspheres with diameters of ~2 μm was coated on top (Figure S5) using a modified Langmuir-Schaefer (LS) self-assembly process, which has been widely used for microparticle deposition. After immobilizing the silica microspheres with a thin PHPS-derived bonding layer, a white paper-like

inorganic emitter was attained. Figure 1d shows a 20 cm×20 cm sample fabricated on a silver-coated aluminum film, as it has excellent optical performance (Figure S6-S8) and is commercially available.

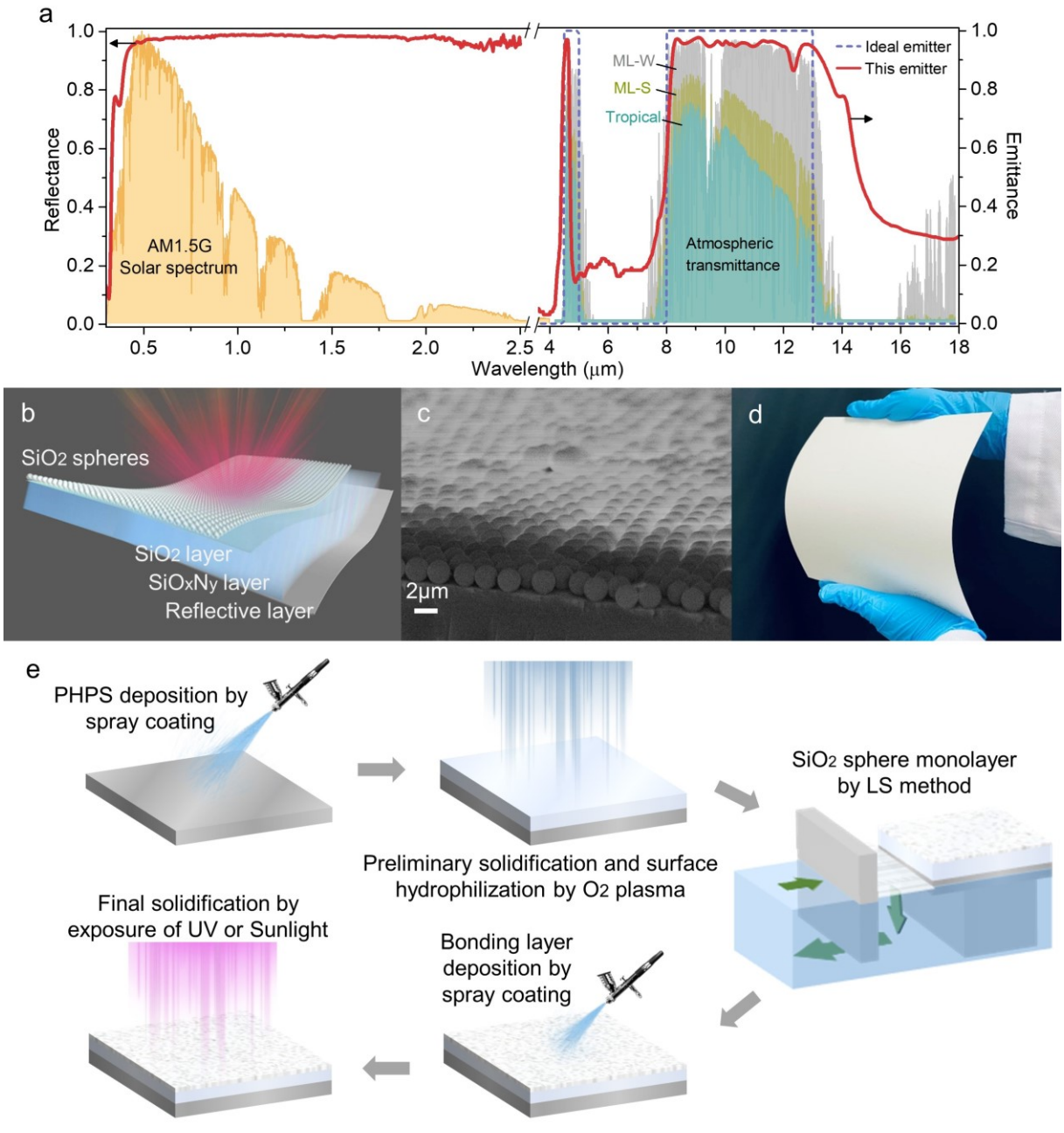

Figure 1 | Spectra and fabrication processes of the inorganic emitter. a, Solar reflective and thermal Emissive spectra of the emitter. Normalized solar irradiation and atmospheric transmittances in different climates (ML-W: mid-latitude winter, ML-S: mid-latitude summer and tropical) were plotted as background. **b,** Schematic, **c,** Scanning electron micrograph and **d,** Photograph of the emitter (20 × 20 cm). **e,** Schematic of fabrication processes of the emitter.

The optical function of each component of the emitter is schematically shown in **Figure 2**a. The SiO_xN_y layer is transparent to sunlight but it generates intrinsic selective emission within the 8-13 μm atmospheric window, because the Si-O bond has vibration peaks at around 8.5, 9.4 and 12.5 μm and the Si-N bond has vibration peak ar around 11 μm.[33] The monolayer of close-packed SiO_2 microspheres above the SiO_xN_y layer further selectively enhances the emissivity at the wavelengths near 9 μm and 12 μm. The normalized emissive power of each part is shown in Supplementary Figure S9. The bottom silver layer can elongate the optical path to improve the emittance within 8-13 μm and produce high reflection beyond the window. The coupling of these three layers leads to strong narrowband IR emission in the atmospheric window ($\varepsilon_{8\text{-}13\mu m}$ = 94.6%) and excellent spectral selectivity (η_ε = 1.46). Also, although the silver layer can provide excellent solar reflectance, strong scatterings of visible light by the microspheres enable the transition from specular to diffusive reflection on the emitter surface (Figure 1d and S10-11). It is important in practical applications to avoid glare appearance and light pollution problems.

The refractive index of the PHPS-derived SiO_xN_y is shown in Figure 2d (upper panel). Owing to the Si-N and Si-O bonds,[30] its extinction coefficient k is quite large between 8 μm and 13 μm but rather small in other regions, resulting in strong emission mainly in the 8-13μm window. Figure 2e (upper panel) illustrates the emissivities of SiO_xN_y layers with different thicknesses on a reflective surface. Within the atmospheric window, its $\varepsilon_{8\text{-}13\mu m}$ rapidly rises to around 80% when the thickness increases to 2 μm, and then only slightly improves with the increasing thicknesses. Beyond the atmospheric window, the average emissivity keeps increasing with the increasing layer thickness because of the non-zero k value. The highest selectivity (η_ε = 2.2) is achieved at a thickness of ~0.6 μm but the corresponding $\varepsilon_{8\text{-}13\mu m}$ is small; further increasing the thickness will gradually reduce the selectivity to ~1.1 (Figure S12). Thus, if the layer thickness is controlled between 1.5 and 4 μm, the PHPS-derived emitter can offer both a high emissivity ($\varepsilon_{8\text{-}13\mu m}$ > 80%) and high selectivity (η_ε > 1.4). This large

thickness tolerance provides great opportunities for cost reduction in large-scale fabrication, compared to previous photonic or plasmonic structures with nanometer-level tolerance.

The $\varepsilon_{8\text{-}13\mu m}$ of a single SiO_xN_y layer can reach ~80%, but it is difficult to be further improved without sacrificing the selectivity η_ε through increasing the thickness, because of the reflection peaks at around 9 and 12 μm caused by the Reststrahlen bands of bulk SiO_xN_y. Figure 2e (upper panel) clearly shows weaker emission near 9 and 12 μm due to the Reststrahlen bands for almost all the thicknesses. Different from its bulk counterpart, SiO_2 microspheres show resonance-enhanced light-matter interactions especially at wavelengths of around 9 and 12 μm and therefore high absorption/emission,[22] which is perfectly complementary to the SiO_xN_y layer (Figure 2e (lower panel)). The resonance with strong near-field confinement was identified as surface phonon polaritons (SPhP). Further, the high-intensity near-field effect can be outcoupled into far-field through diffraction by a periodic surface structure and induce emission enhancement.[34] A close-packed monolayer can generate 20% more IR emission than that with randomly distributed spheres of the same size.[35] Compared with non-close-packed SiO_2 microsphere monolayers of different periodicities, a close-packed monolayer shows the strongest resonance absorption (Figure S13). Meanwhile, increasing the number of microsphere layers rapidly broadens the emission spectrum. Therefore, a close-packed monolayer of SiO_2 microspheres was deposited on top of SiO_xN_y to selectively enhance $\varepsilon_{8\text{-}13\mu m}$.

The IR selectivity of SiO_2 microspheres strongly relies on their size. Figure 2e (lower panel) shows the emissive spectra of a monolayer of SiO_2 microspheres with different diameters on a reflective surface. When the diameter is larger than 1.6 μm, two strong narrowband emission peaks appear at desired wavelengths (9 μm and 12 μm). When the size exceeds 2.6 μm, higher-order FrÖhlich resonances will be excited beyond the Reststrahlen bands,[18] deteriorating the infrared selectivity. Hence, SiO_2 spheres with sizes of 1.6-2.6 μm are selected to provide complementary emission while keeping the IR selectivity. This is different from previous works using 8-μm SiO_2 microspheres to realize broadband IR emission.[20, 35] Figures 2b-c show that the electric fields at λ = 9.4 μm and 12.5 μm, two vibration peaks of Si-O bond, were enhanced by ten- and six-fold in the gaps among the spheres, which contributes to selective strong emission shown in Figure 2e (lower panel). While for the wavelengths at 8 and 11.5 μm, two vibration valleys of Si-O bond within 8-13 μm, only weak electric field enhancement can be observed around the spheres (Figure S14), corresponding to weak emission regions of the SiO_2 microspheres monolayer.With the complementary coupling of SPhP with

the selective emission spectrum of the SiO_xN_y layer, the microsphere-enhanced emitter shows a much-improved IR emissivity ($\varepsilon_{8\text{-}13\mu m}$ = 94.6%) at a near-normal angle while maintaining a high η_ε of 1.46 (Figure 1a). The measured angular emittance also illustrates a cutoff around 70° zenith angle, which matches the optimal value for directional emitter with selective emission to maximize the cooling temperature[36] (Figure S15).

When PHPS is annealed at low temperatures (< 300 ºC), the film is slightly hydrophobic due to low dispersive and polar forces.[30] The contact angle of the PHPS-derived SiO_xN_y layer near room temperature is close to 90° (Figure 2f). However, after depositing a monolayer of hydrophobic microspheres, the surface became more hydrophobic and the water contact angle reached ~130° (Figure 2g). Such hydrophobic surfaces endow the emitters with water-repelling behaviors and self-cleaning capability, which may benefit their operation and maintenance in harsh outdoor environments.

WILEY-VCH

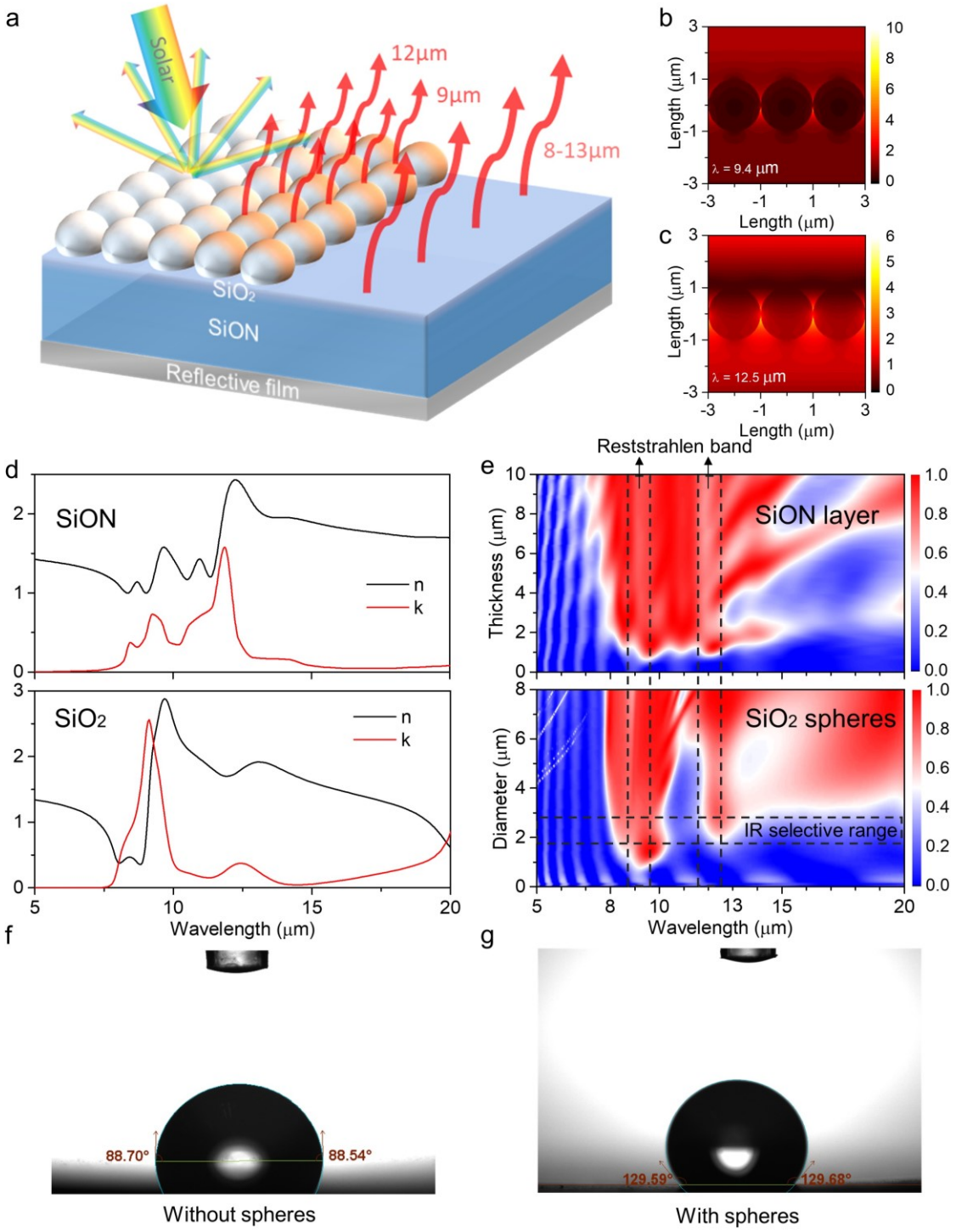

Figure 2 | Optical properties of the emitter. a, The optical structure of the emitter. **b-c**, Electric field enhancement at 9.4 μm (b) and 12.5 μm (c) by polariton resonance. **d**, Refractive index and extinction coefficient of bulk silicon oxynitride (upper panel) and silicon dioxide (lower panel) **e**, Calculated emissive spectra for silicon oxynitride (upper panel) and close-packed SiO_2 sphere monolayer (lower panel) on a reflective surface as functions of the layer thickness and sphere size, respectively. **f-g**, The water contact angles of the PHPS-derived emitter without (f) and with (g) the silica microsphere monolayer.

2.2. The Outdoor Experiment in a Subtropical Coastal City (Hong Kong)

Two field tests were conducted at noontime in a relatively less humid autumn month, November (average RH=72%), and a humid summer month, July (average RH=81%),[37] on the roof of a seaside building in Hong Kong (Figure S16). The experimental setup is shown in **Figures 3**a-b. A 4-inch emitter was directly mounted on the top of a cubic high-density expanded polystyrene (EPS) foam without adopting any solar shading or convective cover (the so-called roof cooling mode). The EPS has strong solar reflection (R_{solar} = 92.3%) higher than aluminum foil (R_{solar} = 90.1%) and commercial heat-reflective white paints (R_{solar} = 85.9%) (Figure S17) and its thermal conductivity are only 0.035 W m^{-1} k^{-1},[38] which can minimize the absorbed heat transferring from the foam to the emitter. Type-T thermocouples were attached to the backside of the emitter via a small tunnel penetrating through the foam. To accurately measure the ambient air temperature, the heating from the concrete ground and the direct exposure of the thermometer under sunlight should be avoided, which might cause overestimation of the ambient air temperature and in turn the cooling temperature by at least 2-3 °C according to our tests. Here we used a well-calibrated commercial weather station standing beside with a shutter box kept at the same height level as the emitter (about 1 meter from the floor) to accurately measure the ambient air temperature, relative humidity, solar irradiation and wind speed simultaneously. The comparision for the emitters with and without convective cover was also investigated in Figure S18.

In the November test, the sky was clear with an average cloud coverage of 11% (5th November, 2019).[37] The measured temperatures of ambient air and the emitters together with the solar irradiation are shown in Figure 3d. The mean solar irradiation (I_{solar}), relative humidity (RH) and wind speed (WS) during the noontime were 740 W m^{-2}, 43% and 0.6m s^{-1}, respectively. The emitter

exhibited up to 5 °C cooling below the ambient air and it maintained a stable substrate temperature even when the wind speed increased to above 1 m s^{-1}. In the nighttime, the relative humidity rose up to about 80%, while the wind speed decreased to 0.2m s^{-1}. About 6 °C subambient cooling was still achieved by the emitter, as shown in Figure 3e. The corresponding nonradiative heat transfer coefficient was calculated to be ~10 W m^{-2} K^{-1}, agreeing well with the empirical formula attained by Zhao et al.[8] Continuous data were also recorded for the following 2 cloudy days with the cloud coverages of 47% and 32%, respectively (Figure S19). The temperature drop of the emitter decreased to 1-2 °C at noontime, while it could still be maintained at 1-4 °C under RH value up to 90%.

July in Hong Kong is normally very hot and humid (mean T_{air} > 28 °C and mean RH > 80%). The summer test was conducted on 9th July 2021, when the sky was cloudy with an average cloud coverage of 28%.[37] A commercial heat-reflective white paint, which has a R_{solar} of 85.9% and $\varepsilon_{8\text{-}13}$ of 93.7%, was used as a reference in the test for comparison (Figure 3c). Although the $\varepsilon_{8\text{-}13}$ of the white paint is close to our emitter, it is a non-selective broadband emitter with a spectral selectivity around 1 (Figure S20). The environmental data and the temperatures of the emitters near noontime are shown in Figure 3f. The peak solar irradiation was above 1000 W m^{-2}. The mean relative humidity was 59% and the ambient air temperature was about 33.5 °C at noontime, and the PWV was estimated to be about 43 mm,[39] which is higher than the threshold for tropical climate defined in MODTRAN.[40] This PWV value is consistent to the real-time data recorded by CIMSS through microwave-frequency sensors.[41] The emitter exhibited up to 2.5 °C cooling at noontime. For the white paint, no cooling was observed during the test and the temperature rose up to around 8 °C higher than the ambient temperature (Figure 3f). In the nighttime, the RH increased to around 80% and the ambient temperature changed to 28.5 °C, corresponding to a PWV of 44 mm. Both emitter and white paint showed cooling effects due to their high $\varepsilon_{8\text{-}13}$ and their temperatures were fluctuating due to the moving cloud. The IR-selective emitter achieved up to 5 °C sub-ambient cooling and its cooling temperature was consistently 40% larger than that of the non-selective white paint (Figure 3g). All the results illustrate an outstanding cooling performance of our inorganic IR-selective emitter in hot humid climates.

A comparative study of roof cooling was also conducted using two wooden model houses (60×70×85 cm) with a standard thermal insulating roof and an emitter-assembled roof, respectively. Figures 3h-i show the visible and IR image of the houses at noontime (the ambient temperature was ~31 °C). Due to the variation in surface orientation and sidewall heating by sunlight, the emitter roof temperature

varied with position and the lowest temperature could reach 24 °C. In contrast, the temperature of the standard roof ranged from 55 °C to 67°C. The average air temperature inside the house with the cooling roof was ~8 °C and 2 °C lower than that of the reference house at daytime and nighttime, respectively (Figure S21). Besides, a 20×20 cm emitter was mounted on top of a 200-ml water container to cool water. Subambient water cooling of up to 7 °C and 3 °C were observed at nighttime and noontime, respectively (Figure S22). These tests show the great potential of this emitter for space cooling.

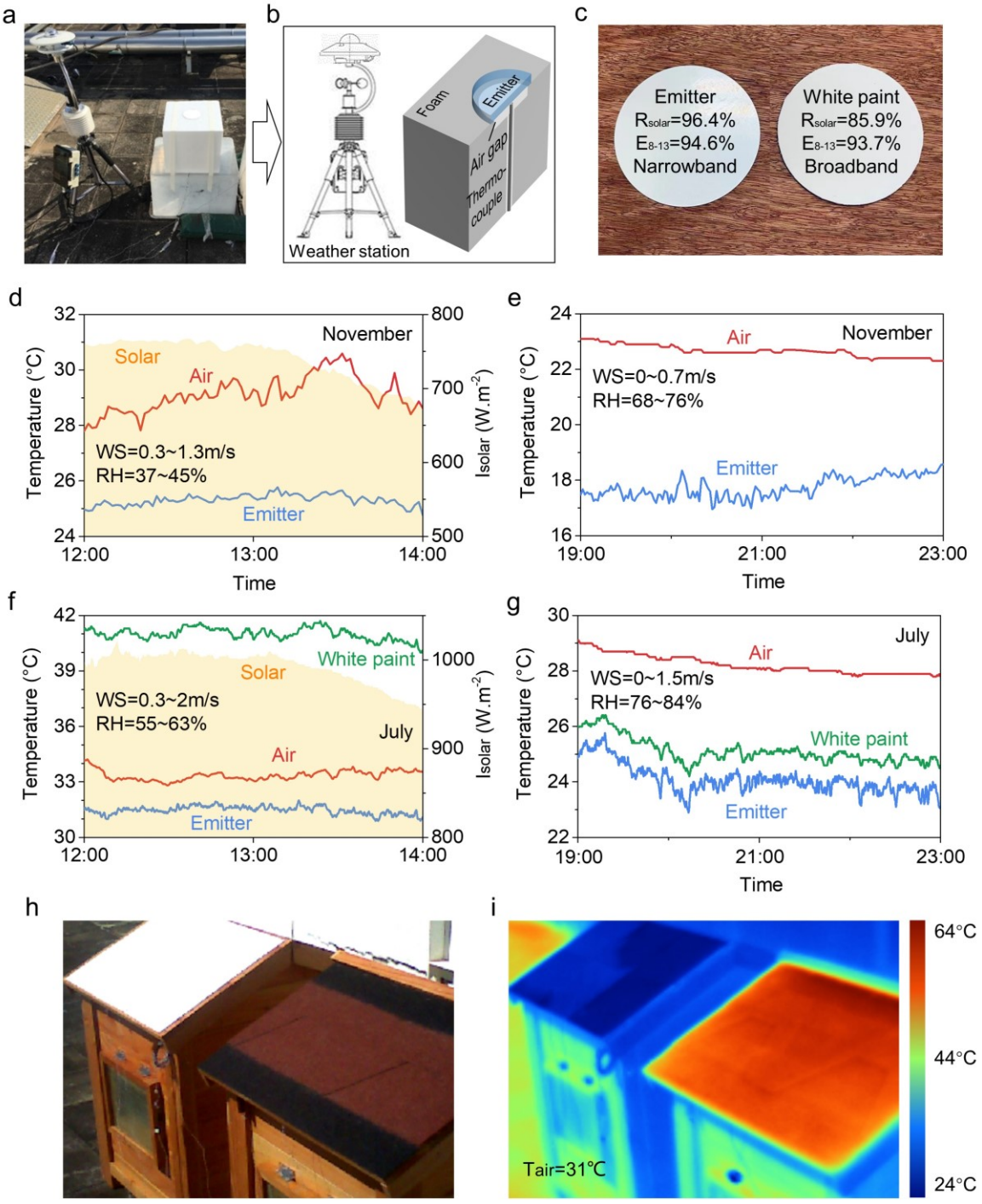

Figure 3 | Outdoor experiment in a subtropical coastal city (Hong Kong). a, Picture of the setup with an emitter on the EPS foam. **b,** Schematic of the platform (b). **c**, Photograph of the emitter and a

commercial heat reflective white paint. **d-e**, Measured solar irradiation and temperatures of the ambient air and the emitter at noontime (d) and nighttime (e) in November of Hong Kong. **f-g**, Measured solar irradiation and temperatures of the ambient air, the emitter and white paint at noontime (f) and nighttime (g) in July of Hong Kong. The orange shade indicates the solar irradiation. **h-i**, Visible (h) and IR (i) photographs of two wooden model houses (60×70×85 cm) with a standard thermal insulating roof and an emitter-assembled roof under direct sunlight at noontime in November of Hong Kong.

2.3. Cooling Performance and Durability Evaluation of the Emitters

Most emitters in the literature show high solar reflectance (> 94%), but their infrared emissive spectra are quite different. Two indexes have been proposed to quantify the selectivity and cooling capability of a radiative surface,[8] i.e., the weighted emissivity $\varepsilon_{8\text{-}13\mu m}$ over the 8-13 μm window at T_{amb} = 300 K and the spectral selectivity η_ε. Since the secondary atmospheric windows only slightly contribute to the cooling performance, $\varepsilon_{8\text{-}13\mu m}$ can indicate the emission power of an emitter and η_ε indicates the ratio of the surface emission to the absorption from the ambient, i.e., the capability in achieving a high cooling temperature in different climates.[9, 42] The $\varepsilon_{8\text{-}13\mu m}$ and η_ε of various emitters for daytime cooling[2, 17, 19-21, 23, 24, 43-52] were calculated based on their spectra and plotted in **Figure 4**a. Most emitters with an $\varepsilon_{8\text{-}13\mu m}$ above 90% show a relatively low selectivity η_ε (< 1.1), indicating their broadband emitter nature. So far, the highest η_ε (1.48) was achieved by the photonic emitter developed by Raman et al.,[2] which showed an $\varepsilon_{8\text{-}13\mu m}$ of 65%. Our emitter exhibits strong solar reflection (96.4%), high IR emission ($\varepsilon_{8\text{-}13\mu m}$ = 94.6%) and outstanding selectivity (η_ε = 1.46), showing a performance closest to an ideal selective emitter compared to state-of-the-art emitters (Figure 4a). The cooling performance of the emitter in six typical climates from MODTRAN 6 was evaluated and compared with those of an ideal selective emitter and ideal IR-broadband emitter (Figure S23). Our emitter's behavior is close to that of the ideal selective emitter and has a bigger potential of cooling temperature than the ideal broadband emitter in different climates, illustrating its excellent cooling performance and climate applicability.

The noontime cooling powers of some of the best-reported emitters in tropical conditions defined by MODTRAN[40] are also compared in Table S1. This value is the comprehensive result from both solar reflectance and surface emittance, indicating how fast the emitters will cool down in the initial state,

which is different from the balanced cooling temperature. Since the atmospheric windows are small and narrow in tropical climate (Figure S1), all noontime cooling powers are smaller than 18 W/m^2, which is consistent with the limit shown in Figure S23. Our emitter illustrates cooling power of 16 W/m^2. It is slightly smaller than the power (16.4 W/m^2) of a hierarchically porous polymer emitter reported by Mandal,[23] while obviously higher than those of other emitters (most are below 10 W/m^2).

The durability of daytime radiative emitters is crucial for long-term operation. UV exposure by sunlight and water immersion by rain are two main challenges for maintaining emitters' cooling performances in practical applications. UV can break some chemical bonds in organic materials and in turn modify the spectra, causing degradation and aging problems.[25] Moisture and oxygen can attack the reflective layer through pinholes and induce matrix variation, while some materials with pores can absorb water, which affect their optical properties.[8] The dense all-inorganic structure of our emitter inherently endows it with excellent resistance to UV and water. The Si-O bond energy is larger than the energy of the shortest UV in sunlight (~300 nm) and water cannot pass through or accumulate in the dense hydrophobic SiO_xN_y/silica microsphere structure. To confirm this, we conducted durability tests with the emitter directly exposed to UV and water. A sphere-enhanced emitter was exposed to solar UV for up to 3 equivalent months (720 hours, 8 hours/day) and immersed in water continuously for up to 3 weeks. The spectra were measured before and after the tests for comparison and the results are shown in Figure 4b**.** The spectra of the emitter were almost identical after these tests, illustrating its long-term reliability and high resistance to UV irradiation and water.

After the UV exposure and water immersion, a standard cross-cut tape test (ASTM D3359) was conducted to investigate the adhesion strengths of the SiO_xN_y / Ag interface and SiO_2 spheres / SiO_xN_y layer / Ag interface. Since PHPS-derived ceramic film can generate chemical metal-O-Si bonds with metal surface,[53, 54] no coating spalling happened after the test (Figure 4c) and the adhesion strength of SiO_xN_y / Ag interface was classified as 5B level. For the SiO_2 spheres/ SiO_xN_y interface, the particles were bonded by SiO_xN_y layer and only small flakes were detached at the edges (Figure 4d), thus it has an adhesion level of 4B. Both 5B and 4B ratings are considered as good adhesion.

Bending tests with bending degrees from 30° to 90° were conducted to characterize the flexibility of the emitter (Figure S24). No cracks of the coating were observed until the cracking of substrates (0.3mm aluminium film) happen. The bending durability is limited by the substrates instead of the coating. The emitter is free of cracks for 28, 11 and 6 cycles for 30°, 60° and 90° bending,

respectively. The reduction of solar reflectance caused by cracking is around 1% (Table S2). This flexibility of the emitter can be further improved by changing the substrate. The combined effect of dust and moisture was also evaluated and shown in Figure S25. Although 13%, 4% and 24% reduction of solar reflectance (R_{solar}) were observed after the dust deposition, moisture condensation and dust & moisture deposition, respectively, the R_{solar} recovered after drying of moisture and breezing of dust.

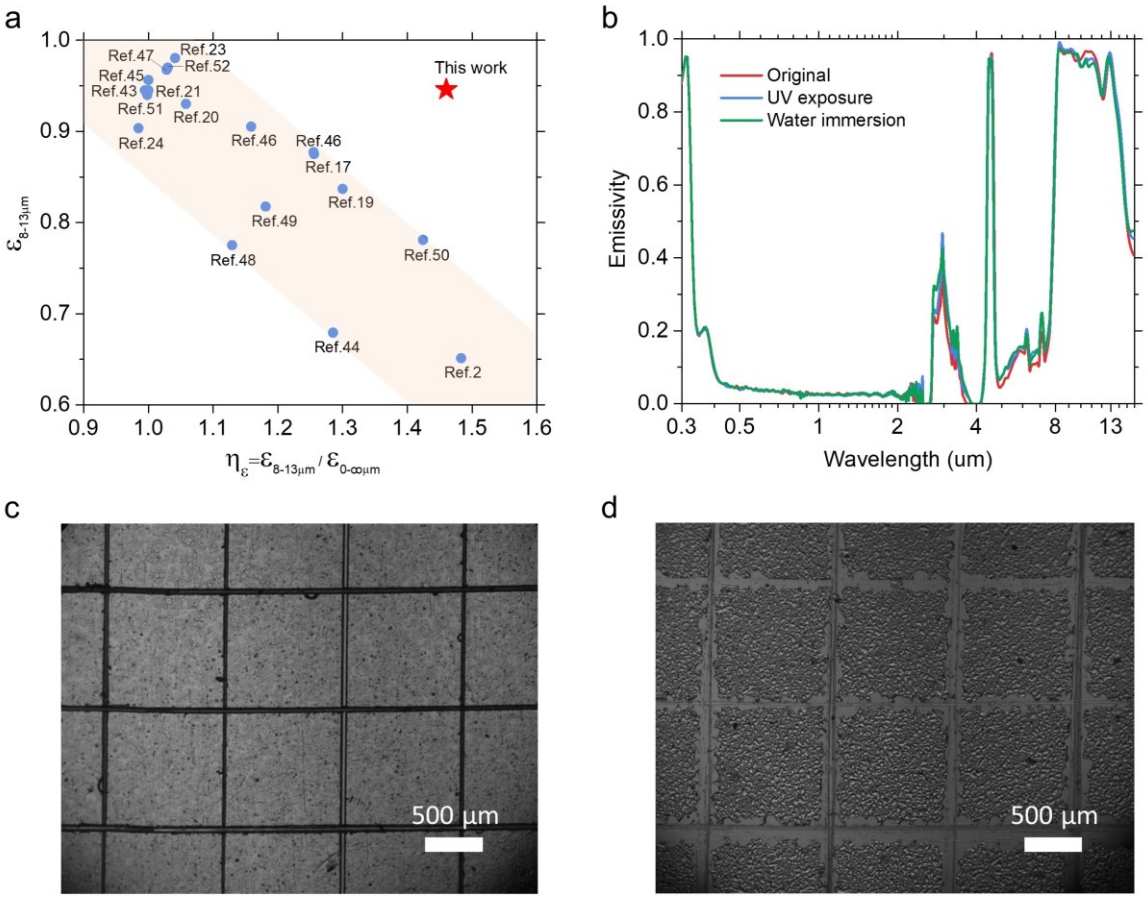

Figure 4 | Cooling potential and reliability of emitters. a, Cooling potentials ($\varepsilon_{8\text{-}13\mu m}$ for cooling power and η_ε for cooling temperature) of recently reported high-performance emitters for daytime radiative cooling and the emitter in this work. **b**, Spectra of the sphere-enhanced emitter before and

after long-term solar UV exposure (3 months) and water immersion (3 weeks). **c-d**, Photographs of samples after standard cross-cut tape test of (c) SiO_xN_y / Ag and (d) SiO2 spheres / SiO_xN_y interfaces.

3. Conclusion

In summary, we have developed an efficient all-inorganic narrowband emitter for daytime radiative cooling. It shows strong solar reflection (96.4%) and highly selective IR emission ($\varepsilon_{8\text{-}13\mu m}$ = 94.6%, η_ε = 1.46) within the atmospheric window, rendering it suitable for radiative cooling in hot humid climates. Its great IR-selective emission is realized by coupling the selective emission of PHPS-derived SiO_xN_y with the narrowband polariton resonance of a monolayer of closely packed silica microspheres. Temperature drops of up to 5 °C in autumn and 2.5 °C in summer were achieved at noontime under high humidity with the emitter directly exposed to the ambient in a subtropical coastal city, Hong Kong. Furthermore, the high-performance emitter was fabricated by scalable solution-based fabrication processes at room temperature, rendering it promising for large-scale deployment. The excellent UV and water resistance of this inorganic emitter also enable its excellent durability in a harsh outdoor environment. In the future, prefabricated products that can be installed on the target outdoor surfaces could be developed. Self-adaptive radiative coolers with dynamically tunable optical performance are also highly desirable for real-world applications.

4. Experimental Section

Sample preparation process: Commercial perhydropolysilazane (PHPS, 20 wt%) was purchased from Iota Silicone Oil (Anhui, China) company as a precursor for the silicon oxynitride layer. A layer of PHPS was deposited onto a silicon or metal substrate coated with 20-nm titanium/120-nm silver by spray coating or spin coating, with thickness control through the concentration of PHPS and flow rate or rotational speed. The samples after the preliminary solidification in ambient air were then put into a plasma treatment system (March PX-250) to be exposed to 55 W oxygen plasma at 0.1 torr for 3 mins to complete surface hydrophilization, prepared for the next Langmuir-Schaefer (LS) process. The film was dried and put on a holder immersing inside a water-filled LS trough. Hydrophobic silica spheres were spread and compressed to a monolayer floating on the water surface. The water was pumped out until the water level was below the film to deposit a monolayer of silica spheres on the surface. Thereafter, a low-concentration PHPS (5 wt%, diluted by N-tincyl ether) was sprayed or spin-coated

onto the silica sphere monolayer to bond the silica sphere monolayer to the silicon oxynitride film. Finally, the samples were naturally solidified in the air or accelerated solidified by UV/solar irradiation at room temperature.

Characterizations: The morphologies of the fabricated samples were checked by Scanning Electron Microscopy (SEM, JSM-6390, JEOL) equipped with energy dispersive X-ray spectroscopy (EDX). The confirmation of composition from the cross-section of samples was carried out by the EDX method. The depth profiling analysis of the silicon oxynitride layer was conducted by X-ray Photoelectron Spectroscopy (XPS, PHI 5600 multi-technique system, Physical Electronics) in conjunction with ion beam sputtering and Time-of-Flight Secondary Ion Mass Spectrometry (ToF-SIMS, Physical Electronics 7200 ToF-SIMS spectrometer). For accurate characterization, a silicon wafer was used as the substrate and 20-nm titanium and 120-nm silver were deposited as adhesive and reflective layers respectively by e-beam evaporation (Peva-450E). The UV-visible-NIR (0.3-2.5 μm) reflectance spectra of the emitters were measured using a spectrometer (Lambda 950, Perkin Elmer) equipped with a 150 mm integrating sphere. The mid-infrared emissive spectra were calculated from the reflectance spectra measured by Fourier transform infrared spectrometer (FTIR, Vertex 70, Bruker) with a gold-coated integrating sphere (PIKE Technologies). An angle adjustor was used for both spectrometers to measure angular reflection, from which angular emissive spectra can be gained. The water contact angles were measured by a contact angle meter (Biolin Theta).

Solar reflectance calculation: The spectrally averaged solar reflectance R_{solar} was defined as:

$$R_{solar} = \frac{\int_{0.3\mu m}^{3\mu m} R(\lambda) E_{solar}(\lambda) d\lambda}{I_{solar}} \qquad (1)$$

Here $E_{solar}(\lambda)$, $R(\lambda)$ and I_{solar} represent the spectral solar power (AM 1.5G), the spectral reflectance of surfaces at the wavelength λ, and total solar power, respectively.

Weighted emissivity and thermal spectral selectivity calculation: The weighted emissivity $\varepsilon_{8\text{-}13\mu m}$ and the spectral selectivity η_{ε} were defined as:

$$\varepsilon_{a-b\mu m} = \frac{\int_{a\mu m}^{b\mu m} d\lambda I_{BB}(\lambda, T_{amb}) \varepsilon(\lambda)}{\int_{a\mu m}^{b\mu m} d\lambda I_{BB}(\lambda, T_{amb})} \qquad (2)$$

$$\eta_{\varepsilon} = \frac{\varepsilon_{8-13\mu m}}{\varepsilon_{0-\infty\mu m}} \quad (3)$$

Here I_{BB} and $\varepsilon(\lambda)$ represent the blackbody spectral radiance at the ambient temperature T_{amb} =300K and spectral emissivity of the emitters. The calculations for the emitter in this work was based on the measured emissive spectrum while for emitters reported in the literature, the calculations were based on their reported spectra.

Numerical simulations of the emitter: The spectrum simulations for the structures were performed using a commercial finite-difference time-domain (FDTD) method (Lumerical software).

Calculation of cooling performance: The cooling power was defined as:

$$P_{cool}(T_{emitter}, T_{amb}) = P_{rad}(T) - P_{atm}(T_{amb}) - P_{solar} - P_{nonrad}(T_{emitter}, T_{amb}) \quad (4)$$

where P_{rad} is the radiative power from the emitter surface, P_{solar} and P_{atm} are the absorbed radiation power from sunlight and atmosphere, respectively, and P_{nonrad} is the nonradiative heat transfer rate. $T_{emitter}$ is the temperature of the emitter and T_{amb} is the temperature of ambient air. The maximum cooling power was attained when $T_{emitter}$ = T_{amb}. The maximum cooling temperature ΔT_{max} was defined as ΔT_{max} = T_{amb} -$T_{emitter}$ when P_{cool} = 0.

Cooling performance measurements: The ambient data, including the ambient temperature, solar irradiation, relative humidity and wind speed, were measured by a calibrated commercial portable weather station (Wuhan Yigu Chenyun Technology Co., Ltd, YG-BX). The emitters' temperatures were measured using T-type thermocouples connected to a high-density thermocouple module (NI 9213 16 TC).

Ultraviolet resistance tests: The samples were put in a test box with two 40 W UV lamps installed inside. The irradiation of these UV lamps peaks at 340 nm, which works as a solar ultraviolet simulator. The reflective spectra of samples were measured before and after the long-term (up to 720 hours) UV exposure.

Supporting Information

Supporting Information is available from the Wiley Online Library or from the author.

Acknowledgements

This work was financially supported by Bright Dream Robotics of Country Garden (UB-19.005). We also thank the support from the Hong Kong Research Grant Council (RGC) via General Research Fund (GRF) account 16200518 and Collaborative Research Fund (CRF) account C6022-16G, respectively. The authors thank Prof. Ronggui Yang at Huazhong University of Science and Technology, China, for the helpful discussions. C. Lin and Y. Li contributed equally to this work.

Conflict of Interest

The authors declare no competing interests.

Received: ((will be filled in by the editorial staff))
Revised: ((will be filled in by the editorial staff))
Published online: ((will be filled in by the editorial staff))

References

[1] S. Catalanotti, V. Cuomo, G. Piro, D. Ruggi, V. Silvestrini, G. Troise, *Sol. Energy.* **1975***, 17*(2), 83-89.

[2] A. P. Raman, M. A. Anoma, L. Zhu, E. Rephaeli, S. Fan, *Nature.* **2014***, 515*(7528), 540-544.

[3] J. Liu, D. Zhang, S. Jiao, Z. Zhou, Z. Zhang, F. Gao, *Sol. Energy Mater Sol. Cells.* **2020***, 208*, 110412.

[4] D. Han, B. F. Ng, M. P. Wan, *Sol. Energy Mater Sol. Cells.* **2020***, 206*, 110270.

[5] J. Khedari, J. Waewsak, S. Thepa, J. Hirunlabh, *Renew. Energ.* **2000***, 20*(2), 183-193.

[6] C. Y. Tso, K. C. Chan, C. Y. Chao, *Renew. Energ.* **2017***, 106*, 52-61.

[7] S. Y. Jeong, C. Y. Tso, Y. M. Wong, C. Y. Chao, B. Huang, *Sol. Energy Mater Sol. Cells.* **2020***, 206*, 110296.

[8] D. Zhao, A. Aili, Y. Zhai, S. Xu, G. Tan, X. Yin, R. Yang, *Appl. Phys. Rev.* **2019**, *6*(2), 021306.

[9] C. G. Granqvist, A. Hjortsberg, T. S. Eriksson, *Thin Solid Films.* **1982**, *90*(2), 187-190.

[10] Z. Chen, L. Zhu, A. Raman, S. Fan, *Nat. Commun.* **2016**, *7*, 1-5.

[11] M. Hossain, M. Gu, *Adv. Sci.* **2016**, *3*(7).

[12] Y. Li, C. Lin, J. Huang, C. Chi, B. Huang, *Global Challenges.* **2021**, *5*(1), 2000058.

[13] M. Zeyghami, D. Y. Goswami, E. Stefanakos, *Sol. Energy Mater Sol. Cells.* **2018**, *178*, 115-128.

[14] X. Sun, Y. Sun, Z. Zhou, M. A. Alam, P. Bermel, *Nanophotonics.* **2017**, *6*(5), 997-1015.

[15] S. Vall, A. Castell, *Renew. Sust. Energ. Rev.* **2017**, *77*, 803-820.

[16] B. Zhao, M. Hu, X. Ao, N. Chen, G. Pei, *Appl. Energy.* **2019**, *236*, 489-513.

[17] D. Chae, M. Kim, P. Jung, S. Son, J. Seo, Y. Liu, B. J. Lee, H. Lee, *ACS Appl. Mater. Interfaces.* **2020**, *12*(7), 8073-8081.

[18] K. Yao, H. Ma, M. Huang, H. Zhao, J. Zhao, Y. Li, S. Dou, Y. Zhan, *ACS Applied Nano Materials.* **2019**, *2*(9), 5512-5519.

[19] H. Ma, K. Yao, S. Dou, M. Xiao, M. Dai, L. Wang, H. Zhao, J. Zhao, Y. Li, Y. Zhan, *Solar Energy Mater. Solar Cells.* **2020**, *212*, 110584.

[20] Y. Zhai, Y. Ma, S. N. David, D. Zhao, R. Lou, G. Tan, R. Yang, X. Yin, *Science.* **2017**, *355*(6329), 1062-1066.

[21] S. Atiganyanun, J. B. Plumley, S. J. Han, K. Hsu, J. Cytrynbaum, T. L. Peng, S. M. Han, S. E. Han, *ACS Photonics.* **2018**, *5*(4), 1181-1187.

[22] H. Bao, C. Yan, B. Wang, X. Fang, C. Y. Zhao, X. Ruan, *Sol. Energy Mater Sol. Cells.* **2017**, *168*, 78-84.

[23] J. Mandal, Y. Fu, A. C. Overvig, M. Jia, K. Sun, N. N. Shi, H. Zhou, X. Xiao, N. Yu, Y. Yang, *Science.* **2018**, *362*(6412), 315-319.

[24] T. Li, Y. Zhai, S. He, W. Gan, Z. Wei, M. Heidarinejad, D. Dalgo, R. Mi, X. Zhao, J. Song, *Science.* **2019**, *364*(6442), 760-763.

[25] H. Zweifel, *Stabilization of polymeric materials*, Springer Science & Business Media**2012**.

[26] A. Morlier, S. Cros, J. Garandet, N. Alberola, *Thin Solid Films.* **2012***, 524*, 62-66.

[27] 久保朋子, 幸塚広光, *Journal of the Ceramic Society of Japan (日本セラミックス協会学術論文誌).* **2006***, 114*(1330), 517-523.

[28] C. R. Blanchard, S. T. Schwab, *J Am Ceram Soc.* **1994***, 77*(7), 1729-1739.

[29] H. Matsuo, O. Funayama, T. Kato, H. Kaya, T. Isoda, *Journal of the Ceramic Society of Japan.* **1994***, 102*(1185), 409-413.

[30] K. Wang, M. Günthner, G. Motz, B. D. Flinn, R. K. Bordia, *Langmuir.* **2013***, 29*(9), 2889-2896.

[31] T. S. Eriksson, C. G. Granqvist, *Appl. Opt.* **1983***, 22*(20), 3204-3206.

[32] T. S. Eriksson, S. Jiang, C. G. Granqvist, *Solar Energy Materials.* **1985***, 12*(5), 319-325.

[33] Y. Jeong, C. Pearson, H. Kim, M. Park, H. Kim, L. Do, M. C. Petty, *ACS applied materials & interfaces.* **2016***, 8*(3), 2061-2070.

[34] J. Greffet, R. Carminati, K. Joulain, J. Mulet, S. Mainguy, Y. Chen, *Nature.* **2002***, 416*(6876), 61-64.

[35] J. Jaramillo-Fernandez, G. L. Whitworth, J. A. Pariente, A. Blanco, P. D. Garcia, C. Lopez, C. M. Sotomayor-Torres, *Small.* **2019**, 1905290.

[36] S. Jeon, J. Shin, *Optics Express.* **2021***, 29*(6), 8376-8386.

[37] Hong Kong Observatory, Climate and weather of Hong Kong, www.hko.gov.hk/en/index.html.

[38] Á Lakatos, F. Kalmár, *Mater. Struct.* **2013***, 46*(7), 1101-1105.

[39] C. Ruckstuhl, R. Philipona, J. Morland, A. Ohmura, *Journal of Geophysical Research: Atmospheres.* **2007***, 112*(D3).

[40] A. Berk, J. van den Bosch, F. Hawes, T. Perkins, P.F. Conforti, G.P. Anderson, R.G. Kennett, P.K. Acharya, **2018**.

[41] Chris Valden Anthony Wimmers, MIMIC-TPW Version 2, http://tropic.ssec.wisc.edu/real-time/mtpw2/about.html.

[42] C. G. Granqvist, A. Hjortsberg, *J. Appl. Phys.* **1981**, *52*(6), 4205-4220.

[43] J. Kou, Z. Jurado, Z. Chen, S. Fan, A. J. Minnich, *ACS Photonics.* **2017**, *4*(3), 626-630.

[44] G. J. Lee, Y. J. Kim, H. M. Kim, Y. J. Yoo, Y. M. Song, *Adv. Opt. Mater.* **2018**, *6*(22), 1800707.

[45] X. Wang, X. Liu, Z. Li, H. Zhang, Z. Yang, H. Zhou, T. Fan, *Adv. Funct. Mater.* **2020**, *30*(5), 1907562.

[46] A. Aili, Z. Y. Wei, Y. Z. Chen, D. L. Zhao, R. G. Yang, X. B. Yin, *Mater. Today Phys.* **2019**, *10*, 100127.

[47] H. Zhang, K. C. Ly, X. Liu, Z. Chen, M. Yan, Z. Wu, X. Wang, Y. Zheng, H. Zhou, T. Fan, *Proc. Natl. Acad. Sci. U. S. A.* **2020**, *117*(26), 14657-14666.

[48] E. Rephaeli, A. Raman, S. Fan, *Nano Lett.* **2013**, *13*(4), 1457-1461.

[49] C. Zou, G. Ren, M. M. Hossain, S. Nirantar, W. Withayachumnankul, T. Ahmed, M. Bhaskaran, S. Sriram, M. Gu, C. Fumeaux, *Adv. Opt. Mater.* **2017**, *5*(20), 1700460.

[50] D. Li, X. Liu, W. Li, Z. Lin, B. Zhu, Z. Li, J. Li, B. Li, S. Fan, J. Xie, J. Zhu, *Nat. Nanotechnol.* **2021**, *16*(2), 153-158.

[51] S. Zeng, S. Pian, M. Su, Z. Wang, M. Wu, X. Liu, M. Chen, Y. Xiang, J. Wu, M. Zhang, *Science.* **2021**, *373*(6555), 692-696.

[52] T. Wang, Y. Wu, L. Shi, X. Hu, M. Chen, L. Wu, *Nat. Commun.* **2021**, *12*(1), 1-11.

[53] M. Günthner, T. Kraus, A. Dierdorf, D. Decker, W. Krenkel, G. Motz, *J. Eur. Ceram. Soc.* **2009**, *29*(10), 2061-2068.

[54] M. Günthner, T. Kraus, W. Krenkel, G. Motz, A. Dierdorf, D. Decker, *Int. J. Appl. Ceram. Technol.* **2009**, *6*(3), 373-380.

[55] G. Barroso, M. Döring, A. Horcher, A. Kienzle, G. Motz, *Adv. Mater. Interfaces.* **2020**, *7*(10), 1901952.

[56] B. Zhao, X. Li, M. Hu, X. Ao, Q. Xuan, G. Pei, *Journal of Renewable and Sustainable Energy.* **2020**, *12*(1), 014703.

[57] T. S. Eriksson, C. G. Granqvist, *Appl. Opt.* **1982**, *21*(23), 4381-4388.

The table of contents entry

We utilize different emissive behaviors between a bulk film and particles in Reststrahlen band and achieve an emitter with excellent spectrum selectivity. This emitter successfully realizes good subambient cooling in hot and humid conditions, which is always a challenge for radiative cooling. The all-inorganic components and solution-based fabrication process render it durable and scalable simultaneously.

A Solution-processed Inorganic Emitter with High Spectral Selectivity for Efficient Subambient Radiative Cooling in Hot Humid Climates